Published in final edited form as:

Adv Funct Mater. 2018 August 22; 28(34): . doi:10.1002/adfm.201801787.

Development of Citrate-based Dual-Imaging Enabled Biodegradable Electroactive Polymers

Dingying Shan,
Department of Biomedical Engineering; Materials Research Institute; The Huck Institutes of The Life Sciences The Pennsylvania State University, University Park, PA, 16802, USA

Sri-Rajasekhar Kothapalli,
Department of Biomedical Engineering The Pennsylvania State University, University Park, PA 16802, USA; Penn State Hershey Cancer Institute Hershey, PA 17033, USA

Dino J. Ravnic,
Department of Surgery Penn State Hershey Medical Center, Hershey, PA, 17033, USA

Ethan Gerhard,
Department of Biomedical Engineering; Materials Research Institute; The Huck Institutes of The Life Sciences The Pennsylvania State University, University Park, PA, 16802, USA

Jimin P. Kim,
Department of Biomedical Engineering; Materials Research Institute; The Huck Institutes of The Life Sciences The Pennsylvania State University, University Park, PA, 16802, USA

Jinshan Guo,
Department of Biomedical Engineering; Materials Research Institute; The Huck Institutes of The Life Sciences The Pennsylvania State University, University Park, PA, 16802, USA

Chuying Ma,
Department of Biomedical Engineering; Materials Research Institute; The Huck Institutes of The Life Sciences The Pennsylvania State University, University Park, PA, 16802, USA

Jiazhi Guo,
Biomedical Engineering Research Center Kunming Medical University, Kunming, 650500, China

Li Gui,
Department of Endocrinology The Third People's Hospital of Yunnan Province, Kunming 650011, China

Lin Sun,
Department of Cardiology The Second Affiliated Hospital, Kunming Medical University, Kunming 650101, China

Di Lu,
Biomedical Engineering Research Center Kunming Medical University, Kunming, 650500, China

jxy30@psu.edu, ludi20040609@126.com.

Supporting Information

Supporting Information is available from the Wiley Online Library or from the author.

Jian Yang
Department of Biomedical Engineering; Materials Research Institute; The Huck Institutes of The Life Sciences The Pennsylvania State University, University Park, PA, 16802, USA

Abstract

Increasing occurrences of degenerative diseases, defective tissues and severe cancers heighten the importance of advanced biomedical treatments, which in turn enhance the need for improved biomaterials with versatile theranostic functionalities yet using minimal design complexity. Leveraging the advantages of citrate chemistry, we developed a multifunctional citrate-based biomaterial platform with both imaging and therapeutic capabilities utilizing a facile and efficient one-pot synthesis. The resulting aniline tetramer doped biodegradable photoluminescent polymers (BPLPATs) not only possess programmable degradation profiles (<1 to >6 months) and mechanical strengths (~20 MPa to > 400 MPa), but also present a combination of intrinsic fluorescence, photoacoustic (PA) and electrical conductivity properties. BPLPAT nanoparticles are able to label cells for fluorescence imaging and perform deep tissue detection with PA imaging. Coupled with significant photothermal performance, BPLPAT nanoparticles demonstrate great potential for thermal treatment and *in vivo* real-time detection of cancers. Our results on BPLPAT scaffolds demonstrate three-dimensional (3D) high-spatial-resolution deep tissue PA imaging (23 mm), as well as promote growth and differentiation of PC-12 nerve cells. We envision that the biodegradable dual-imaging-enabled electroactive citrate-based biomaterial platform will expand the currently available theranostic material systems and open new avenues for diversified biomedical and biological applications via the demonstrated multi-functionality.

Graphical Abstract

Multifunctional biodegradable citrate-based biomaterials that integrates dual-modal fluorescence/photoacoustic imaging with electroactivity are developed. The newly developed citrate-based biomaterials demonstrate impressive multi-functionalities, including cell labelling, deep tissue photoacoustic imaging, as well as electroactive and photothermal therapeutics, in a single material setting, offering an enabling tool for diversified biomedical applications such as bioimaging, drug delivery, tissue engineering, and bioelectronics.

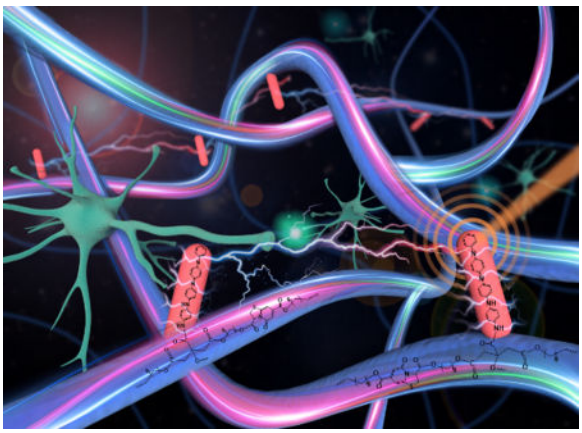

Keywords

citrate; fluorescence; photoacoustic; conductive polymers; degradation

1. Introduction

The past decades have witnessed the rise of biomaterials as an effective tool to redress the insufficiency of traditional drug and surgery based treatments for degenerative diseases, defects, and cancers,[1–3] as biomaterials have become pervasive in surgery, tissue engineering, drug delivery, and medical devices. However, to provide more effective and targeted therapies, there exists a need for novel biomaterials with versatile functionalities (degradability, biocompatibility, mechanical properties, etc.) to fulfill the comprehensive mechano-electro-chemical-biological requirements *in vivo*,[4, 5] While multifunctionality can be achieved by combining materials and additives, such strategies often lead to prohibitive processing complexity and undesired safety concerns, limiting clinical translation.[6] To balance the need for safety, functionality and simplicity, a biomaterial platform with a high degree of designability of chemical, biological, and structural features utilizing efficient synthesis and processing methods is greatly desired.

To address this challenge, researchers have developed a new class of biocompatible and biodegradable citrate-based polyester elastomers (CBEs) by leveraging the reactive nature of citric acid in a cost effective, catalyst free, one pot polycondensation reaction of citric acid and diol monomers.[7,8] The presence of four functional groups per citrate molecule facilitates modification with additional moieties through pendant groups, as well as the generation of crosslinked networks. Citric acid is thus capable of acting as a keystone molecule, leading to a family of citrate-based materials with inherent physical, chemical, and/or biological functionalities, including tunable degradation rates and mechanical strengths, tissue adhesion, antimicrobial, antioxidant, and fluorescence.[9–16] Concurrently, ease of fabrication has allowed widespread applications of citrate-based biomaterials including tissue engineering (bone, skin, blood vessel, etc.),[12, 17, 18] drug delivery, [19] bioimaging,[14, 16] and biosensing. [20–21]

Among these functionalities, bioimaging is a vital component in theranostic systems, as biomaterials that enable *in-situ* imaging can assess material degradation, track drug delivery, and identify particular diseased tissues to treat cancers and degenerative diseases.[22–24] In particular, fluorescence-based imaging modalities provide high temporal resolution and sensitivity, real-time imaging, cost effectiveness, and use of maneuverable instruments. [24–26] We have recently developed a novel family of biodegradable photoluminescent citrate-based polymers (BPLPs),[14] in which the reaction of citric acid and an amino acid forms an intrinsic fluorescent moiety that have been used to track scaffolds and nanoparticles *in-vivo*.[16] The resulting BPLPs demonstrated strong fluorescence properties including high quantum yield, tunable emission and photostability, as well as biodegradability and biocompatibility, providing significant advantages over traditional fluorescent materials that conjugate or encapsulate organic dyes and cytotoxic quantum dots.

Despite these benefits, fluorescence imaging *in-vivo* with BPLPs is limited by low spatial resolution and imaging depths of only a few millimeters.

To overcome the limitations of single modality imaging technologies, multi modal imaging has drawn extensive attention due to its ability to provide more comprehensive spatial, temporal, structural, and high-resolution information.[27–29] Photoacoustic (PA) imaging, for example, may significantly complement fluorescence imaging systems by providing additional contrast, depth penetration, and spatial resolution to generate a 3D structure.[30–32] Therefore in this work, we sought to incorporate conductive aniline tetramer (AT) moieties into BPLPs to create a new family of dual imaging (fluorescence and PA) BPLP-AT elastomers, since conductive polymers such as polyaniline (PANI)[33] and polypyrrole (PPY)[34] have been well demonstrated as PA contrast agents with strong NIR absorption. In addition to dual-modality imaging, the integration of conductive moieties into our BPLP platform imparted significant electroactivity and photothermal properties of the resulting BPLP-AT elastomers, enhancing therapeutic potential through the transfer of chemical, physical, and electrical signals in biological systems to effectively modulate cellular activities.[35–38] Indeed, BPLP-ATs herein demonstrated improved cellular growth and differentiation in PC-12 cells, particularly in response to electrical stimulus, providing significant advantages over traditional conductive polymers that suffer from poor solubility and processability, brittle mechanics, and non-degradability.[39–41]

In contrast to the complex, multi-component design of traditional theranostic systems, we herein introduce a new family of biodegradable citrate-based elastomers that integrates dual-modality diagnostic imaging with electroactive and photothermal therapeutics via a convenient, one-pot polycondensation reaction, enabling a seamless platform with theranostic potential for disease pre-diagnosis, treatment, and post-surgical monitoring.

2. Results and Discussion

2.1. Synthesis of BPLPAT Pre-polymers

An irreversible decrease in electrical conductivity occurs when PANI is subjected to temperature above 100 °C, and in addition, the conductivity becomes unstable at temperatures above 150 °C.[42, 43] In order to keep the balance between the conductivity of AT and reaction effectiveness, BPLPAT pre-polymers were synthesized by the polycondensation reaction of CA, OD, L-cysteine, and AT at 110 °C (Figure S1). With abundant reactive side carboxyl and hydroxyl groups, BPLPAT pre-polymers can be further reacted to form crosslinked polymeric networks (Figure 1a-b), and are expected to present fluorescence and PA properties to enable dual-modality imaging, as well as significant electroactivity to modulate cellular growth and differentiation (Figure 1c). In order to achieve the applicable functionalities of designed BPLPATs, we first verified the structures of the resulting BPLPAT pre-polymers with ATR-FTIR and ^{1}H-NMR. In ATR-FTIR (Figure 1d), the absorption peak at 1705 cm^{-1} represents the ester group (-C(=O)OR), the broad peak at 2936 cm^{-1} (-CH_2-) of the methylene group is from OD, and the absorption peak at 3372 cm^{-1} comes from hydroxyl groups (-OH). The two peaks at 1488 and 1568 cm^{-1} in the spectra of BPLPATs are attributed to the vibration of the quinoid ring and benzene ring from AT. We measured the areas under the absorption peaks of 1488 cm^{-1} (quinoid ring from AT)

and 1705 cm^{-1} (-C(=O)OR) in ATR-FTIR spectra, and calculated their ratios. The result herein suggests that the proportion of AT in BPLPAT pre-polymers gradually increases from BPLP to BPLPAT15%. In ^{1}H-NMR spectra of BPLPATs (Figure 1e), peaks at 1.25 ppm and 1.52 ppm represent -C$\underline{H}_2$- from OD, and the multiple peaks at 2.75 ppm represent -C$\underline{H}_2$- from CA. Two peaks at 5.60 (b) and 7.15 (a) ppm are assigned to the fluorophore formed by a condensation reaction between CA and L-cysteine. Protons (c-t) from AT are represented by multiple peaks between 6.38 and 7.78 ppm. During the synthesis process, OD and AT compete with each other to react with carboxyl groups from CA. By calculating integrals of peaks coming from protons (c-t) from AT and peaks representing -C$\underline{H}_2$- from OD, ratios of AT to OD in pre-polymers were obtained, indicating increased AT content in the obtained pre-polymers from BPLP to BPLPAT15%. Both ATR-FTIR and ^{1}H-NMR results confirmed the successful synthesis of BPLPAT pre-polymers with component ratios as designed.

2.2. Electrochemical Properties and Conductivities of BPLPAT Materials

As electroactivity determines the main biological functionalities of BPLPATs, we performed a systematic study of the electrochemical and conductive properties of BPLPATs using Autolab PGSTAT-302N and UV-2450 spectrometer. In the obtained cyclic voltammogram (CV) curves (Figure 2a), all BPLPAT groups (BPLPAT5%, BPLPAT10%, and BPLPAT15%) present characteristic oxidation and reduction transition peaks of AT. The CV curves of BPLPATs exhibit two oxidation/reduction peaks around 0.38 and 0.69 V, which correspond to AT's structure transition from the leucoemeraldine base state to the emeraldine state, and from the emeraldine state to the pernigraniline state. The UV absorption spectra of AT and BPLPAT10% presented two peaks at around 320 and 590 nm, which are assigned to the π-π^* transition of the benzenoid ring and the excitonic transition from the benzenoid ring to the quinonoid ring, respectively. After doping AT and BPLPAT10% solutions with CSA, two new absorption peaks at about 430 and 800 nm together with a slight blue shift of the benzenoid absorption peak to 308 nm appeared in their spectra due to the formation of delocalized polarons, which indicate the generation of a conductive phase of emeraldine salts (Figure 2b). The results from both CV curves and UV spectra confirmed the favorable electrochemical properties of BPLPATs. The conductivities of the BPLPAT films doped with CSA were increased from 1.06×10^{-7} to 2.94×10^{-6} S cm^{-1} with increasing AT content (Table 1), which fall within an order of conductivities that may sufficiently support the signal transduction and chemical exchange between cells *in vivo*.[41] Thus, the introduction of AT can impart favorable and tunable electrochemical and conductive properties to BPLPAT materials, which makes BPLPATs promising in regulating biological activities such as migration, proliferation, and differentiation and stimulating tissue regeneration.

2.3. *In vitro* Degradation Properties of BPLPAT Materials

As the favorable degradation of BPLPs have been previously demonstrated, we next sought to assess how the introduction of AT into BPLP impacts on the degradation of the resultant polymers. Representatively, *in vitro* degradation studies were conducted on BPLP and BPLPAT10% pre-polymers (Figure 2c), as well as their crosslinked films (Figure 2d). Before crosslinking, BPLP and BPLPAT10% pre-polymers displayed similar degradation rates. After crosslinking, BPLPAT10% films degraded much slower than BPLP films. BPLP films completely degraded within 18 weeks, whereas BPLPAT10% films still had more than

20% mass remaining after 24 weeks. As indicated from the degradation studies, BPLPAT materials presented degradability with fine adjustment of degradation rates ranging from about three weeks to over six months within the formulations investigated. Different tissue regenerations and disease therapies have their own specific time periods, which are expected to be matched by material degradation profiles. Material degradation rates significantly affect cell viability, cell migration, and angiogenesis within tissue regeneration scaffolds.[44] With the adjustability of degradation profiles, the BPLPATs can be designed with optimum degradation rates to meet specific application requirements.

2.4. Mechanical Properties of BPLPAT Films and Scaffolds

As material stiffness is known to significantly influence cellular activity, biomaterials with tissue-specific mechanical properties are essential for *in vivo* applications. We thus performed tensile mechanical tests of our BPLPAT materials (Figure 3). For dry BPLPAT polymer films, initial modulus increased about 80 times from BPLP (5.21 ± 1.15 MPa) to BPLPAT15% (409.24 ± 7.75 MPa) (Figure 3a). The increased AT content also led to increased tensile stress (Figure 3b) accompanied by decreased tensile strain, except for BPLPAT5%, which has comparable strain to BPLP (Figure 3c). The mechanical properties of BPLPAT films were significantly regulated by the addition of AT, also evidenced by the shape of the tensile stress-strain curves (Figure 3g). BPLP, BPLP5%, and BPLPAT10% films all presented classical stress-strain curves of elastomers, while BPLPAT15% presented a curve characteristic of plastic deformation. As wet conditions are important considerations in biological applications, we also investigated the tensile properties of wet films (Figure 3h). After soaking in PBS for 24hrs, all BPLPAT groups exhibited flexible elastic properties. The introduction of AT into BPLP not only increased the initial modulus and the tensile stress of BPLPATs (Figure 3d-e), but also increased their elongation (Figure 3f), which was attributed to the enhanced hydrogen bonding between BPLPAT polymers. In addition, mechanical properties of BPLPAT scaffolds in compression were also tested. The results indicated that the initial modulus and peak stress of BPLPAT scaffolds in compression were also regulated by the addition of AT (Figure 3i-j).

One significant drawback of BPLPs is their poor mechanical strengths, which limited their biomedical applications, whereas the incorporation of the rigid AT structure successfully overcame this problem. By varying AT content in material synthesis, BPLPAT materials with robust and tunable mechanical properties can be developed. Therefore, BPLPATs may be used in diversified applications, from soft tissues, such as skin and nerve, to hard tissues, such as tooth and bone. [45–47]

2.5. Fluorescence and Photoacoustic (PA) Properties of BPLPAT Pre-polymers

Fluorescence and PA properties of BPLPAT pre-polymers were explored to confirm their applicability as dual functional imaging agents. The fluorescence spectra of BPLP and BPLPAT pre-polymer solutions at different concentrations (5, 2.5, 1.25, 0.625, and 0.3125 mg mL^{-1}) were tested (Figure S2a). The dark color introduced by AT caused strong light absorption. Therefore, at the same pre-polymer concentration, the fluorescence intensity of BPLPAT pre-polymer solutions were generally lower than that of BPLP, and decreased with increased ratios of AT/CA (Figure S2b). Notably, the fluorescence intensity of BPLPAT

solutions reached a maximum within the testing concentration range (BPLPAT5% (1.25mg mL^{-1}), BPLPAT10% (1.25mg mL^{-1}), and BPLPAT15% (0.625mg mL^{-1})), while the fluorescence intensity of BPLP solutions increased gradually with increasing concentrations under the same testing condition (Figure S2b). For BPLP solutions, the increased concentrations caused higher fluorophore density but no significant changes of solution color, so higher concentrations had stronger fluorescence intensity compared to less concentrated solutions. In BPLPAT solutions, the increased concentrations not only resulted in densified fluorophores, but also led to more light absorption by the increasingly dark solutions, leading to optimal concentrations for maximum fluorescence intensity. To better understand the fluorescence differences between BPLP and BPLPATs, the fluorescence spectra of BPLP and BPLPAT solutions at a concentration of 1.25 mg mL^{-1} were compared (Figure 4a), which intuitively presents decreased fluorescence intensity with the increase of AT content. In addition, the photostability of BPLP and BPLPAT pre-polymer solutions were studied (Figure S2c), and the results exhibited a decreased photostability of BPLPATs with increased AT content. The fluorescence intensity of BPLP went down by less than 3% after UV light illumination for 3 hrs, while the intensity of BPLPAT15% decreased about 8%. However, all BPLPAT groups were much more stable than the Rhodamine B control, which decreased 25% in intensity.

PA imaging, based on the absorption of optical energy to generate acoustic signals, have significant advantages such as high spatial resolution, deep tissue penetration, high contrast, and non-ionizing radiation.[30–32] Therefore, the PA imaging performance of BPLPATs was next investigated under variable wavelengths (680–920 nm). The quantitative comparison of the PA signal intensities of BPLPAT solutions at different concentrations is shown in Figure 4b. Due to their strong light absorption at the PA testing wavelengths, BPLPAT pre-polymer solutions (BPLPAT5%, BPLPAT10%, and BPLPAT15%) presented distinct PA signals that increased with increased AT ratios and solution concentrations. In contrast, BPLP solutions had poor PA imaging performance, with even the highest solution concentration of 5mg mL^{-1} presenting no significant PA signal. Within the testing wavelength range, BPLPAT pre-polymer solutions had the strongest PA intensity at the excitation wavelength of 680 nm. Representative superimposed ultrasound and PA images of BPLP and BPLPAT pre-polymer solutions at 680 nm are shown in Figure 4d, and are consistent with the quantitative comparison results (Figure 4b) wherein BPLPAT pre-polymers containing the highest proportion of AT (BPLPAT15%) and at highest concentration (5 mg mL^{-1}) exhibited the strongest PA signal.

To further understand the fluorescence and PA dual-imaging properties of BPLPATs, we compared the fluorescence intensity and PA intensity of BPLPAT pre-polymer solutions at the same concentration of 2.5 mg mL^{-1} (Figure 4c). The fluorescence intensity of BPLPAT solutions decreased with increasing AT content, while their respective PA signals increased gradually. Therefore, the introduction of AT in BPLPATs appears to sacrifice the photoluminescence properties (intensity and photostability) to some degree, while enhancing PA imaging in a dose dependent manner. Thus, BPLPATs demonstrated excellent tunability on their dual-imaging properties through molecular design of materials, which enables custom-designing BPLPAT materials based on the required penetration depth, resolution, and sensitivity for different applications.

2.6. Imaging and Photothermal Capabilities of BPLPAT Nanoparticles

In addition to demonstrating powerful material structure and functionality modulation potential, BPLPATs were also amenable to various fabrication techniques, including fabrication into nanoparticles. Using the nano-precipitation method, BPLP, BPLPAT5%, BPLPAT10%, and BPLPAT15% nanoparticles with sizes of 164.3 ± 6.9, 178.2 ± 4.3, 182.6 ± 2.0, and 181.9 ± 5.7 nm were prepared. All nanoparticles exhibited high stability, as demonstrated by their zeta potential values of −55.5 ± 2.0, −60.2 ± 0.6, −59.3 ± 2.8, and −49.1 ± 0.7 mV, respectively (Table 2).

BPLP and BPLPAT nanoparticle cellular uptake by PC-12 cells was conducted to investigate their fluorescence imaging and cell labeling capabilities. The fluorescent images of PC-12 cells with BPLP and BPLPAT nanoparticles were recorded with a fluorescence microscope (Figure 5a). Although BPLPATs had decreased fluorescence intensity compared to BPLP, cells stained with different nanoparticles all presented strong fluorescence. In addition, cells can be imaged with blue, green, and red fluorescence with different excitations, making BPLPAT nanoparticles versatile for cell labeling and imaging.

The PA imaging ability of BPLP and BPLPAT nanoparticles was also studied. In the PA imaging experiment, nanoparticle solutions with different concentrations were first placed in NIR-inactive polyurethane (PU) tubes, kept inside the water medium, to obtain quantitative signal intensities at wavelengths ranging from 680 to 920 nm. The PA intensities of nanoparticle solutions decreased with decreased AT content and decreased concentrations of each nanoparticle group (Figure 5c and S3a). The representative superimposed ultrasound and PA images are presented in Figure 5b, further confirming the above quantitative results. *Ex vivo* deep tissue PA imaging of BPLP and BPLPAT nanoparticles was also conducted with chicken breast tissue (Figure 5d-i). BPLPAT5%, BPLPAT10% and BPLPAT15% nanoparticle solutions at concentrations of 1 and 2 mg mL^{-1} demonstrated excellent PA imaging performance, when imaged through a 5.5 mm thick layer of chicken tissue (Figure 5e). When the thickness of the tissue was increased to 11mm, BPLPAT15% nanoparticle solutions still showed strong PA signals at both concentrations, BPLPAT10% group presented decreased but detectable signals at both concentrations, whereas the PA signals of BPLPAT5% at both concentrations decreased significantly and were almost undetectable. BPLPAT nanoparticles were able to reach a penetration depth of centimeters, and the depth increased with AT content.

In situ thermal ablation is a promising cancer treatment technique in which material mediated local temperature increases are utilized to kill tumor cells following NIR irradiation. The high NIR absorbance of our BPLPAT materials suggested their potential for photothermal therapy. We thus evaluated the time-dependent temperature of our materials as a function of NIR irradiation time (Figure 5j). The original temperature was 22°C, while after irradiation for 6 min, the temperatures of 0.5 mg mL^{-1} of BPLPAT nanoparticle solutions increased dramatically (BPLPAT5% (40.8 °C), BPLPAT10% (47.4 °C), and BPLPAT15% (52.5 °C)), while that of BPLP only increased to 30.5 °C, equivalent to DI water (30.6 °C). In this study, obvious AT content dependent temperature increases of BPLPAT nanoparticles were found under laser irradiation, whereas BPLP nanoparticle solution and pure water showed little change.

Therefore, BPLPAT nanoparticles not only have fluorescence and PA dual imaging properties, but also provide high NIR absorbance coefficients and excellent photothermal performance, rendering them promising nanomaterials for cell labeling and cancer thermal treatments.

2.7. Imaging Capabilities of BPLPAT Scaffolds

The salt leaching method was applied to fabricate cylindrical BPLP and BPLPAT scaffolds with a diameter of 7mm, thickness of 3mm, and interconnected porosity. To obtain their quantitative PA signals, BPLP, BPLPAT5%, BPLPAT10%, and BPLPAT15% scaffolds were embedded inside a piece of agar gel. PA intensities of BPLPAT scaffolds were recorded at wavelengths from 680 to 920 nm (Figure 6b), and PA intensities at 680 nm were quantitatively compared (Figure S3b). Scaffolds with higher AT content exhibit higher PA intensities (BPLPAT15%>BPLPAT10%>BPLPAT5%>BPLP). In Figure 6a, 3D structures from ultrasound images (Figure 6a1), PA images (Figure 6a2), as well as their superimposed images (Figure 6a3) are displayed. BPLP scaffolds showed no noticeable PA signal, while all BPLPAT scaffolds exhibited strong PA images with high contrast. To explore the deep tissue PA imaging capacity of BPLPAT scaffolds, the BPLP, BPLPAT5%, BPLPAT10%, and BPLPAT15% scaffolds were imaged through a ~11 mm and a ~23mm thick chicken breast tissue under 680 nm laser irradiation (Figure 6 c-e). In both experiments, ultrasound contrast of the scaffolds is poor due to lack of mechanical impedance mismatch between the scaffolds and surrounding tissue, highlighting a common disadvantage of ultrasound to image soft biological tissue material (Figure 6f and i). However, the BPLPAT5%, BPLPAT10%, and BPLPAT15% scaffolds provided excellent 3D PA images without any background noise under a ~ 11 mm chicken tissue (Figure 6g). The PA imaging performance of BPLPAT scaffolds declined under a ~ 23 mm of chicken tissue (Figure 6j) with some background signals. The superimposed images of volumetric ultrasound and PA images (Figure 6h and k) of whole scaffolds are clearly presented for BPLPAT5%, BPLPAT10%, and BPLPAT15%. Using fluorescence imaging, it is difficult achieve high resolution and high optical contrast images with such high penetration depths (greater than 1 cm); however, with strong absorption of light in the NIR spectral range, BPLPAT scaffolds were able to generate high optical contrast PA imaging, which provided penetration depth extending to more than 2 cm. In addition, because the differences in optical absorption between materials and surrounding tissues are much larger than those in acoustic impedance, PA imaging offered greater contrast and specificity of materials from surrounding tissues compared to ultrasound imaging. With excellent PA imaging performance, BPLPAT scaffolds may be applied as implant materials for versatile tissue regeneration applications where *in situ* monitoring of their location, degradation, and/or shape variations are desired.

2.8. *In vitro* Cytotoxicity Evaluation

For any materials that are going to be used for *in vivo* applications, it's necessary to assess their toxicities, Therefore, *in vitro* cytotoxicity evaluation for degraded products of BPLP and BPLPAT10% with rat pheochromocytoma (PC-12) cells was conducted before *in vivo* evaluation (Figure 7a). Degradation products of polymers at various concentration (1×:0.1g mL^{-1}; 5×:0.02g mL^{-1}; 10×:0.01g mL^{-1}; 50×:0.002g mL^{-1}; and 100×:0.001g mL^{-1}) were tested. PLLA was used as control. At the highest concentration of 0.1g mL^{-1}, the

degradation products from all groups (PLLA, BPLP, BPLPAT5%, BPLPAT10%, and BPLPAT15%) showed high toxicity, with cell viability of around (PLLA and BPLP) or lower than (BPLPAT5%, BPLPAT10%, and BPLPAT15%) 20%. When the concentration was reduced to 0.02 g mL^{-1}, the cell viability of PLLA, BPLP and BPLPAT5% groups were over 80%. BPLPAT10% and BPLPAT15% groups showed slightly lower cell viabilities of around 70%. However, when the concentration was reduced to 0.01g mL^{-1}, the cell viabilities of all testing groups were higher than 85%, which demonstrated that the diluted degradation products were nontoxic. From the toxicity study, we can see that more incorporated AT caused higher cellular toxicity at very concentrated conditions; however, as shown above, BPLPATs only degrade slowly. The local concentrations of their degradation products are expected to remain in the safe window *in vivo*, which can be confirmed by the excellent *in vivo* host response data presented below.

2.9. *In vitro* Cell Proliferation and Electrical Stimulation

In order to test the effects of electrical functionalities of BPLPAT materials on cellular activities, PC-12 cells were cultured on a series of BPLPAT films (BPLP, BPLPAT5%, BPLPAT10%, and BPLPAT15%) up to 7 days (Figure 7b). BPLPAT films significantly promoted the proliferation of PC-12 cells when compared with BPLP, which might be caused by the electroactive properties. However, with increased AT content, BPLPAT10% and BPLPAT15% films showed slightly reduced cell proliferation rate compared to BPLPAT5%, likely caused by the toxicity of more AT released over time. *In vitro* cell culture studies confirmed the cytocompatibility of BPLPAT films, as well as their capability for the promotion of PC-12 proliferation.

Conductive materials are capable of transferring electrical signals among cells. Therefore, we applied electrical fields to BPLPAT films and investigated the differentiation behavior of the cultured PC-12 cells (Figure 7e). In this experiment, BPLP, BPLPAT5%, BPLPAT10%, and BPLPAT15% films were studied, and films without electrical stimulation were used as controls. After electrical stimulation, cell morphologies were studied with SEM (Figure 7f). Without electrical stimulation, PC-12 cells cultured on BPLP films mostly kept their original spindle shape, whereas cells on BPLPAT films formed multiple neurites along each cell body. The morphologies of PC-12 cells on BPLP films didn’t show obvious differences from those without electrical stimulation; however, cells on BPLPAT films changed dramatically after electrical stimulation evidenced by the long and branched neurites along their cell bodies. Therefore, BPLPAT films themselves were able to stimulate neurite formation due to their inherent electrical conductivity, and the addition of external electrical stimulation strongly promoted the growth and elongation of neurites. BPLP, BPLPAT5%, BPLPAT10%, and BPLPAT15% scaffolds were also used for PC-12 cell growth and differentiation under electrical stimulation. SEM images show that PC-12 cells were able to cover the surface and penetrate deep into the porous scaffold (Figure 7g). Moreover, the branched and extended neurites indicate that cells that grew on BPLPAT scaffolds displayed improved differentiation. Therefore, BPLPAT scaffolds will be great candidates for nerve regeneration applications.

2.10. *In vivo* Foreign Body Response Studies on BPLPAT Films

In vivo foreign body response of BPLPAT films was studied via a subcutaneous implantation study of BPLP, BPLPAT5%, and BPLPAT10% in SD rats using PLLA as control. All samples implanted for 1 week produced a slight acute inflammatory response, expected with the introduction of a foreign material into the body and confirmed by cell infiltration (H & E staining, Figure S4) as well as the appearance of CD11b positive cells (CD11b staining, Figure S5) in the tissues surrounding the polymer films. After 8 weeks of implantation, a thin fibrous capsule between all sample films and muscle were formed, indicating minimal inflammatory reactions. Quantitative cell counting study indicated that total cell densities and CD11b positive cell densities surrounding different polymer film implants declined over time (Figure 7c and d). Interestingly, BPLPAT5% and BPLP10% films exhibited less total cell densities and CD11b positive cell densities at each time point. After 24 weeks of implantation, most of the cells surrounding the implanted samples were fibroblast cells. CD11b positive cells were rarely seen after 24 weeks, indicating that minor chronic inflammatory reaction took place and the degradation products over time did not cause noticeable toxicity. The mild inflammatory response suggested that BPLPAT films and their degradation products present more favorable host responses than the controls, BPLP and PLLA. These studies demonstrated that BPLPAT materials are biocompatible and safe as implant materials or devices for long-term *in vivo* applications.

3. Conclusion

In this study, we developed a biodegradable multifunctional citrate-based biomaterial, BPLPAT, through a facile and efficient polycondensation reaction. The obtained BPLPAT materials demonstrated intrinsic dual-modal fluorescence/PA imaging capability, electrical conductivity, tunable mechanical properties, and programmable degradation profiles. BPLPAT polymers were fabricated into films, scaffolds, and nanoparticles exemplify their excellent processability. Dual imaging capabilities enabled detection of BPLPAT nanoparticles as well as 3D imaging for BPLPAT scaffolds under deep tissue. BPLPAT nanoparticles demonstrated great photothermal performance due to their high NIR absorbance coefficient. Favorable electroactivity successfully enabled BPLPAT films and scaffolds to promote proliferation and differentiation of PC-12 cells. It is our belief that the unique combination of material properties in one setting including fluorescence imaging and labeling of cells, PA imaging, and electroactivity of the fully degradable BPLPAT makes the polymer an enabling tool for diversified biomedical and biological applications including tissue engineering, imaging, drug delivery, and cancer treatment. Furthermore, the citrate-based biomaterial platform is able to incorporate versatile functional chemicals, biological molecules, or drugs to fulfill specific medical requirements, serving as a powerful tool to enable more personalized and effective medical treatments.

Supplementary Material

Refer to Web version on PubMed Central for supplementary material.

Acknowledgements

The authors would like to acknowledge financial support from National Institutes of Health (USA) awards (CA182670, EB024829, to J.Y.), National Institutes of Health-National Institute of Biomedical Imaging and Bioengineering (USA) award (R00EB017729–04, to S.R.K), National Natural Sciences Foundation of China (81460210, to D.L.), National Natural Sciences Foundation of China (81460173, to L.G.), National Natural Sciences Foundation of China (81560050, to L.S.), and Department of Science and Technology of Yunnan Province (2017FA035, to D.L.). The authors also thank Fuji-VisualSonics and its technical team (Andrew Heinmiller and Kelly O'Connell) for their help with photoacoustic imaging experiments.

References

[1]. Peppas NA, Langer R, Science 1994, 263, 1715. [PubMed: 8134835]

[2]. Langer R, Tirrell DA, Nature 2004, 428, 487. [PubMed: 15057821]

[3]. Huebsch N, Mooney DJ, Nature 2009, 462, 426. [PubMed: 19940912]

[4]. Webber MJ, Khan OF, Sydlik SA, Tang BC, Langer R, Ann. Biomed. Eng 2015, 43, 641. [PubMed: 25201605]

[5]. Webber MJ, Appel EA, Meijer EW, Langer R, Nat. Mater 2016, 15, 13. [PubMed: 26681596]

[6]. Mooney DJ, Darnell M, Nat. Mater 2017, 16, 6365.

[7]. Tran RT, Yang J, Ameer GA, Annu. Rev. Mater. Res 2015, 45, 277. [PubMed: 27004046]

[8]. Ma C, Gerhard E, Lin Q, Xia S, Armstrong AD, Yang J, Bioactive Mater 2018, 3, 19.

[9]. Guo J, Xie Z, Tran RT, Xie D, Jin D, Bai X, Yang J, Adv. Mater 2014, 26, 1906. [PubMed: 24375469]

[10]. Shan D, Zhang C, Kalaba S, Mehta N, Kim GB, Liu Z, Yang J, Biomaterials 2017, 143, 142. [PubMed: 28802101]

[11]. Guo J, Kim GB, Shan D, Kim JP, Hu J, Wang W, Hamad FG, Qian G, Rizk EB, Yang J, Biomaterials 2017, 112, 275. [PubMed: 27770631]

[12]. Guo J, Wang W, Hu J, Xie D, Gerhard E, Nisic M, Shan D, Qian G, Zheng S, Yang J, Biomaterials 2016, 85, 204. [PubMed: 26874283]

[13]. van Lith R, Gregory EK, Yang J, Kibbe MR, Ameer GA, Biomaterials 2014, 35, 8113. [PubMed: 24976244]

[14]. Yang J, Zhang Y, Gautam S, Liu L, Dey J, Chen W, Mason RP, Serrano CA, Schug KA, Tang L, PNAS 2009, 106, 10086. [PubMed: 19506254]

[15]. Hu J, Guo J, Xie Z, Shan D, Gerhard E, Qian G, Yang J, Acta Biomater 2016, 29, 307. [PubMed: 26463014]

[16]. Xie Z, Zhang Y, Liu L, Weng H, Mason RP, Tang L, Nguyen KT, Hsieh JT, Yang J, Adv. Mater 2014, 26, 4491. [PubMed: 24668888]

[17]. Xie D, Guo J, Mehdizadeh MR, Tran RT, Chen R, Sun D, Qian G, Jin D, Bai X, Yang J, J. Mater. Chem 2015, 3, 387.

[18]. Su LC, Xu H, Tran RT, Tsai YT, Tang L, Banerjee S, Yang J, Nguyen KT, ACS nano 2014, 8, 10826. [PubMed: 25222570]

[19]. Li J, Tian Y, Shan D, Gong A, Zeng L, Ren W, Xiang L, Gerhard E, Zhao J, Yang J, Wu A, Biomaterials 2017, 116, 106. [PubMed: 27914983]

[20]. Kim JP, Xie Z, Creer M, Liu Z, Yang Chem J. Sci 2017, 8, 550.

[21]. Zhang C, Kim JP, Creer M, Yang J, Liu Z, Biosens. Bioelectron 2017, 97, 164. [PubMed: 28595077]

[22]. Michalet X, Pinaud FF, Bentolila LA, Tsay JM, Doose S, Li JJ, Sundaresan G, Wu AM, Gambhir SS, Weiss S, Science 2005, 307, 538. [PubMed: 15681376]

[23]. Weissleder R, Nat. Biotechnol 2001, 19, 316. [PubMed: 11283581]

[24]. Artzi N, Oliva N, Puron C, Shitreet S, Artzi S, Bon Ramos A, Groothuis A, Sahagian G, Edelman ER, Nat. mater 2011, 10, 704. [PubMed: 21857678]

[25]. Fan Z, Sun L, Huang Y, Wang Y, Zhang M, Nat. Nanotechnol 2016, 11, 388. [PubMed: 26751169]

[26]. Sita TL, Kouri FM, Hurley LA, Merkel TJ, Chalastanis A, May JL, Ghelfi ST, Cole LE, Cayton TC, Barnaby SN, Sprangers AJ, Savalia N, James CD, Lee A, Mirkin CA, Stegh AH, PNAS 2017, 114, 4129. [PubMed: 28373576]

[27]. Cheng L, Liu J, Gu X, Gong H, Shi X, Liu T, Wang C, Wang X, Liu G, Xing H, Bu W, Sun B, Liu Z, Adv. Mater 2014, 26, 1886. [PubMed: 24375758]

[28]. Olson ES, Jiang T, Aguilera TA, Nguyen QT, Ellies LG, Scadeng M, Tsien RY, PNAS 2010, 107, 4311. [PubMed: 20160077]

[29]. Li K, Liu B, Chem. Soc. Rev 2014, 43, 6570. [PubMed: 24792930]

[30]. Knox HJ, Hedhli J, Chan J, Khalili K, Dobrucki LW, Kim TW, Nat. commun 2017, 8, 1794. [PubMed: 29176550]

[31]. Moon H, Kumar D, Kim H, Sim C, Chang JH, Kim JM, Kim H, Lim DK, ACS nano 2015, 9, 2711. [PubMed: 25751167]

[32]. Pu K, Shuhendler AJ, Jokerst JV, Mei J, Gambhir SS, Bao Z, Rao J, Nat. Nanotechnol 2014, 9, 233. [PubMed: 24463363]

[33]. Wang J, Yan R, Guo F, Yu M, Tan F, Li N, Nanotechnology 2016, 27, 0957.

[34]. Liang X, Li Y, Li X, Jing L, Deng Z, Yue X, Li C, Dai Z, Adv. Funct. Mater 2015, 25, 1451.

[35]. Guimard NK, Gomez N, Schmidt CE, Prog. Polym. Sci 2007, 32, 876.

[36]. Qazi TH, Rai R, Boccaccini AR, Biomaterials 2014, 35, 9968.

[37]. Uppalapati D, Boyd BJ, Garg S, Travas-Sejdic J, Svirskis D, Biomaterials 2016, 111, 149. [PubMed: 27728814]

[38]. Yang G, Kampstra KL, Abidian MR, Adv. Mater 2014, 26, 4954. [PubMed: 24719293]

[39]. Guo B, Glavas L, Albertsson AC, Prog. Polym. Sci 2013, 38, 1263.

[40]. Xie M, Wang L, Guo B, Wang Z, Chen YE, Ma PX, Biomaterials 2015, 71, 158. [PubMed: 26335860]

[41]. Wu Y, Wang L, Guo B, Shao Y, Ma PX, Biomaterials 2016, 87, 18. [PubMed: 26897537]

[42]. Neoh KG, Kang ET, Khor SH, Tan KL, Polym. Degrad. Stab 1990, 27, 107.

[43]. Boeva ZA, Sergeyev VG, Polym. Sci. Ser. C 2014, 56, 144.

[44]. Sung HJ, Meredith C, Johnson C, Galis ZS, Biomaterials 2004, 25, 5735. [PubMed: 15147819]

[45]. Holzapfel GA, The handbook of materials behavior models 2001, 3, 1049.

[46]. Osterhoff G, Morgan EF, Shefelbine SJ, Karim L, McNamara LM, Augat P, Injury 2016, 47, S11.

[47]. Fung YC, Springer Science & Business Media 2013.

[48]. Zhang Y, Tran RT, Qattan IS, Tsai YT, Tang L, Liu C, & Yang J, Biomaterials 2013, 34, 4048. [PubMed: 23465824]

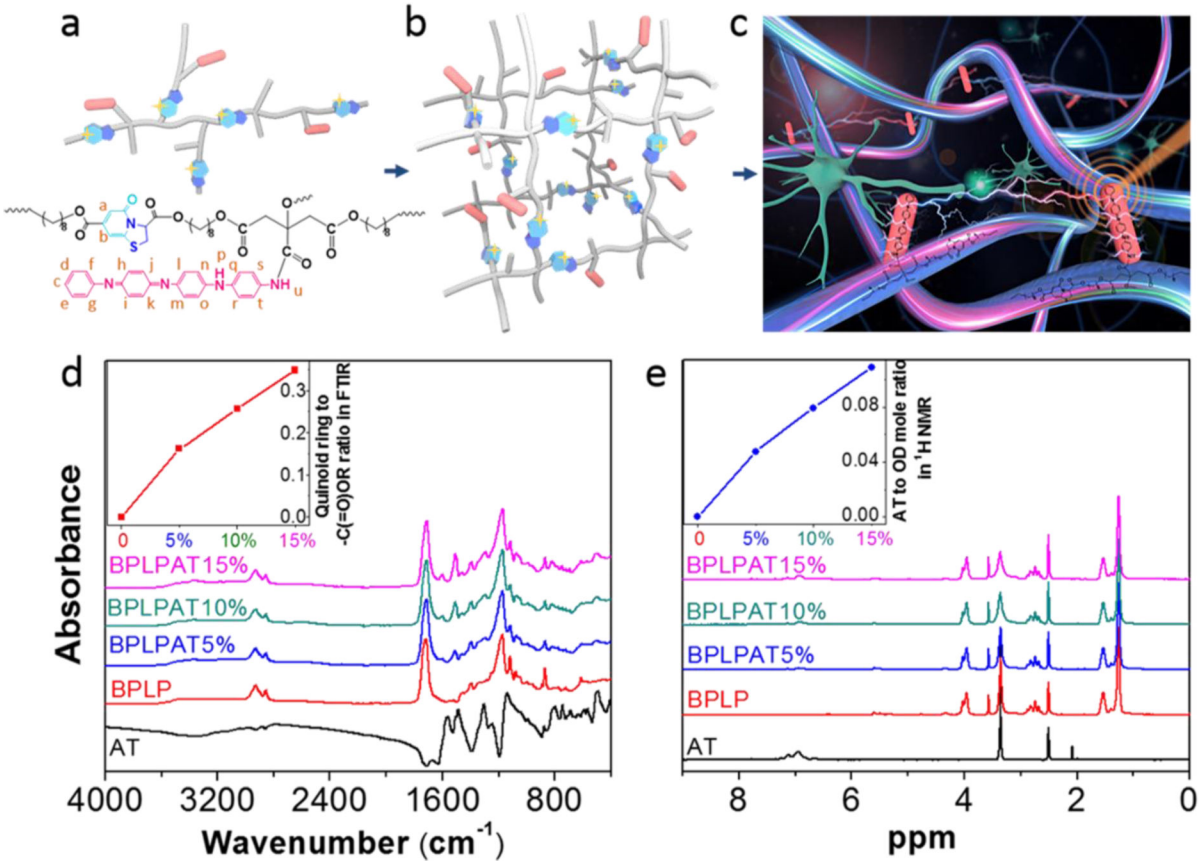

Figure 1.

Characterization of BPLPAT polymer structure. (a) Schematic and chemical structure of BPLPAT pre-polymers. (b) Schematic of crosslinked BPLPAT structure. (c) Schematic of functionalities (fluorescence imaging, PA imaging, and conductivity that promotes cell communications) of crosslinked BPLPATs. (d) ATR-FTIR spectra of AT, BPLP, and BPLPAT pre-polymers. Insert: quinoid ring to -C(=O)OR ratios increase with the increasing concentration of AT in polymer syntheses. (e) ^{1}H NMR spectrum of AT, BPLP, and BPLPAT pre-polymers. Insert: AT to OD molar ratios increase with the increasing concentration of AT in polymer syntheses.

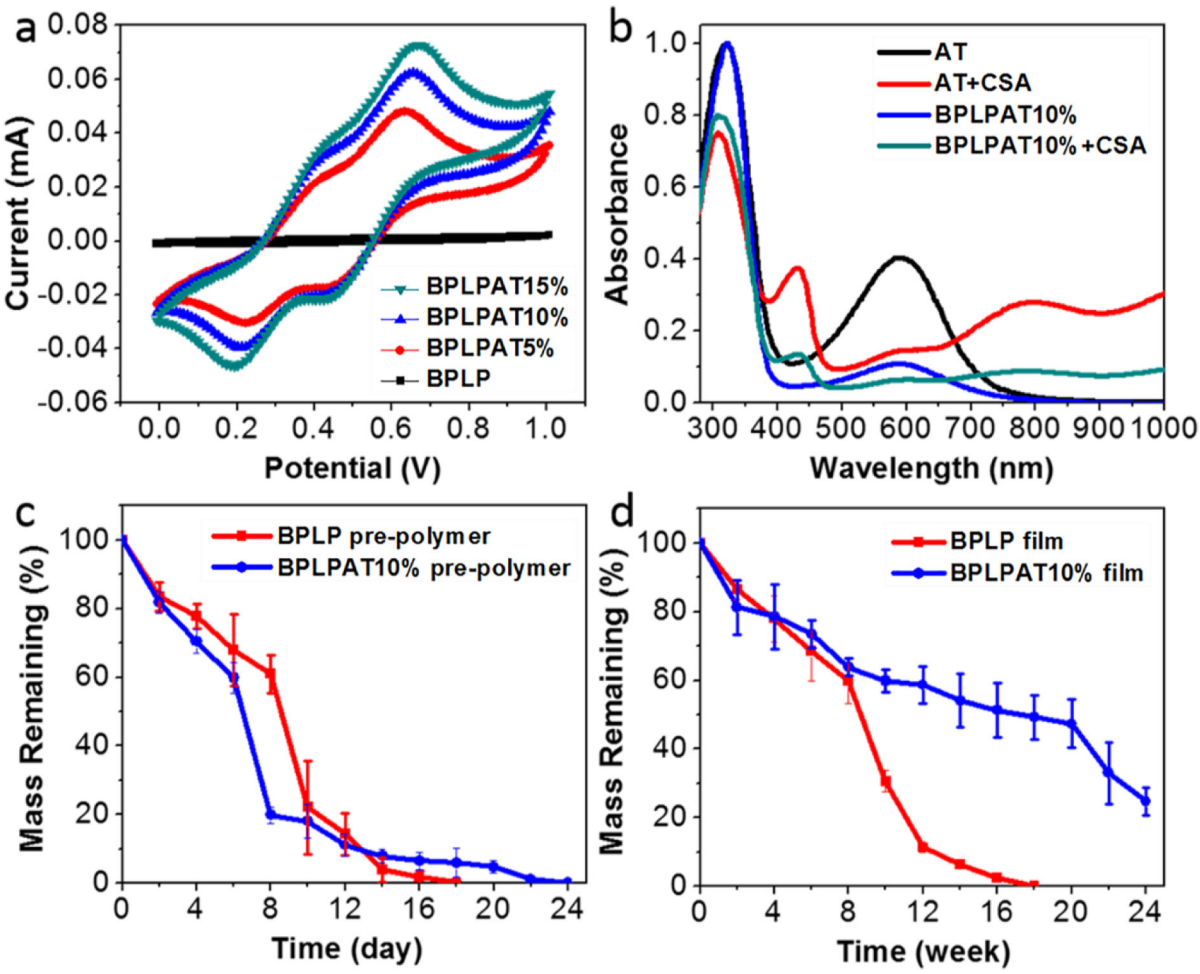

Figure 2.

Electrochemical properties and *in vitro* degradation properties of BPLPATs. (a) The cyclic voltammogram (CV) curves of BPLP and BPLPATs doped with CSA. (b) The UV spectra of AT, CSA doped AT, BPLPAT10%, and CSA doped BPLPAT10%. (c) *In vitro* degradation of BPLP and BPLPAT10% pre-polymers. (d) *In vitro* degradation of BPLP and BPLPAT10% films.

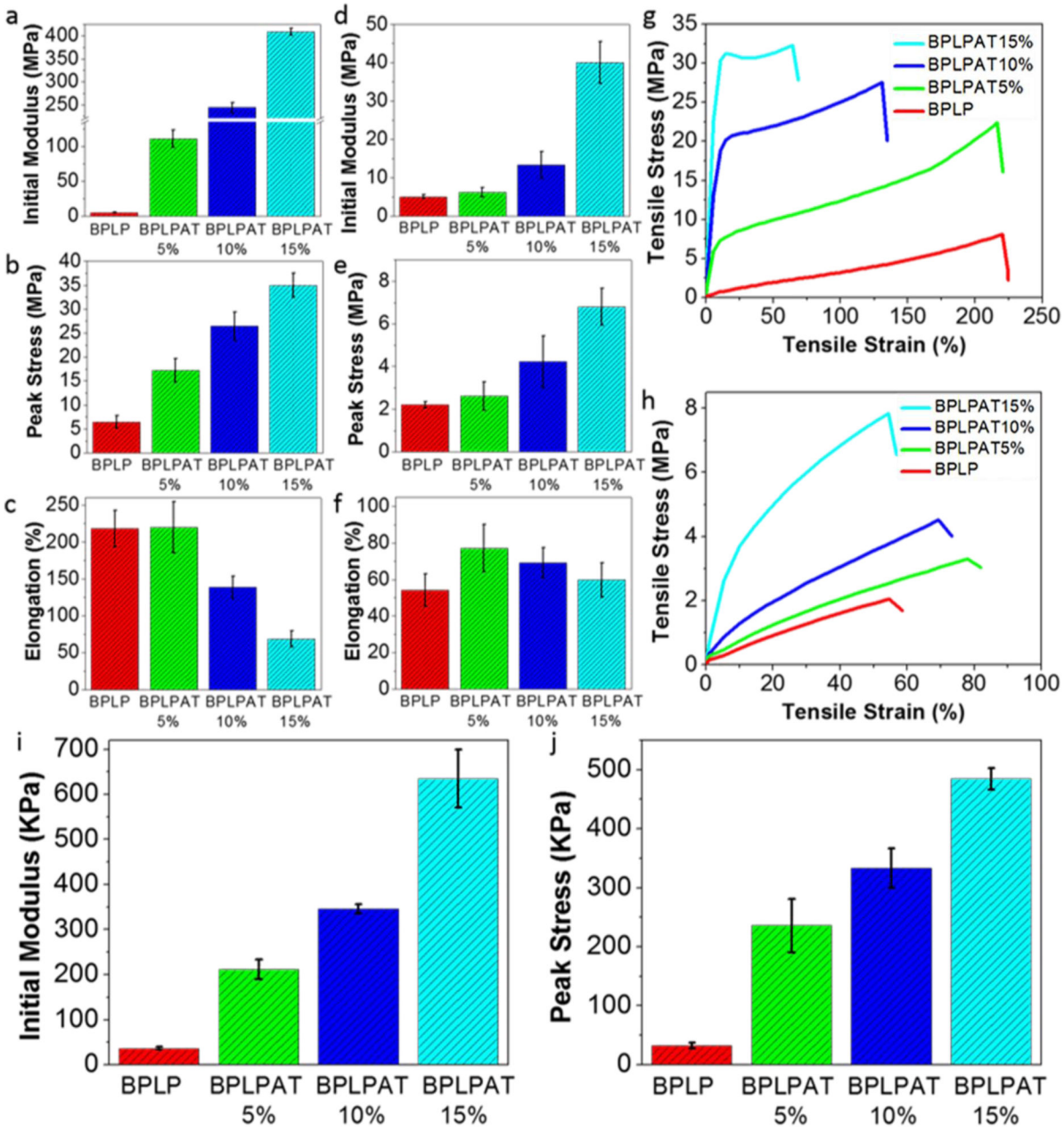

Figure 3.

Mechanical properties of BPLPAT films and scaffolds. (a) Initial modulus, (b) peak stress, and (c) elongation of BPLP and BPLPAT films under dry condition. (d) Initial modulus, (e) peak stress, and (f) elongation of BPLP and BPLPAT films under wet condition. (g) Tensile-Strain curves of BPLP and BPLPAT films under dry condition. (h) Tensile-Strain curves of BPLP and BPLPAT films under wet condition. (i) Initial Modulus and (j) peak stress of BPLP and BPLPAT scaffolds under wet condition.

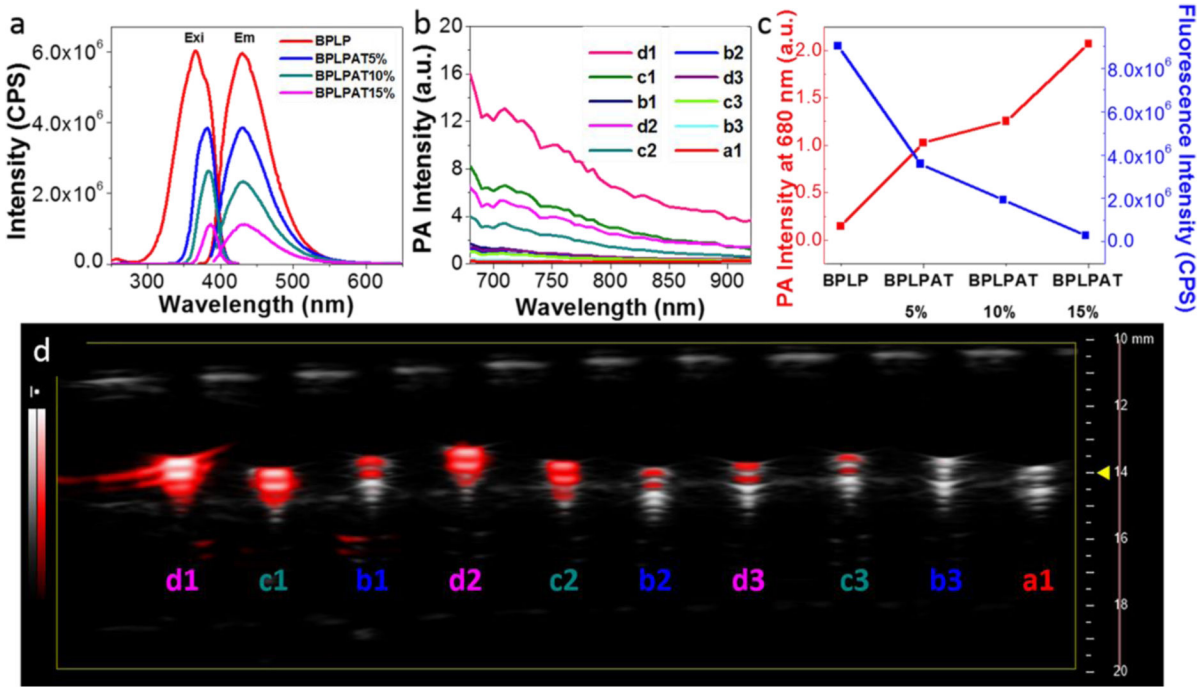

Figure 4.

Fluorescence and PA properties of BPLPAT prepolymer solutions. (a) Fluorescence intensity spectra of BPLP and BPLPAT pre-polymers in dioxane at 1.25 mg/mL. (b) PA intensity of BPLP and BPLPAT pre-polymer solutions in dioxane at various concentrations (5mg/mL, 2.5mg/mL, 0.625mg/mL). (c) PA intensity and fluorescence intensity comparison of BPLP and BPLPAT solutions at 2.5mg/ml. (d) Representative superimposed ultrasound (gray-scale) and PA (pseudo-red scale) images of BPLP and BPLPAT pre-polymer solutions at various concentrations. (BPLPAT15% 5mg/mL(d1), BPLPAT10% 5mg/mL(c1), BPLPAT5% 5mg/mL(b1), BPLPAT15% 2.5mg/mL(d2), BPLPAT10% 2.5mg/mL(c2), BPLPAT5% 2.5mg/mL(b2), BPLPAT15% 0.625mg/mL(d3), BPLPAT10% 0.625mg/mL(c3), BPLPAT5% 0.625mg/mL(b3), BPLP 5mg/mL(a1).

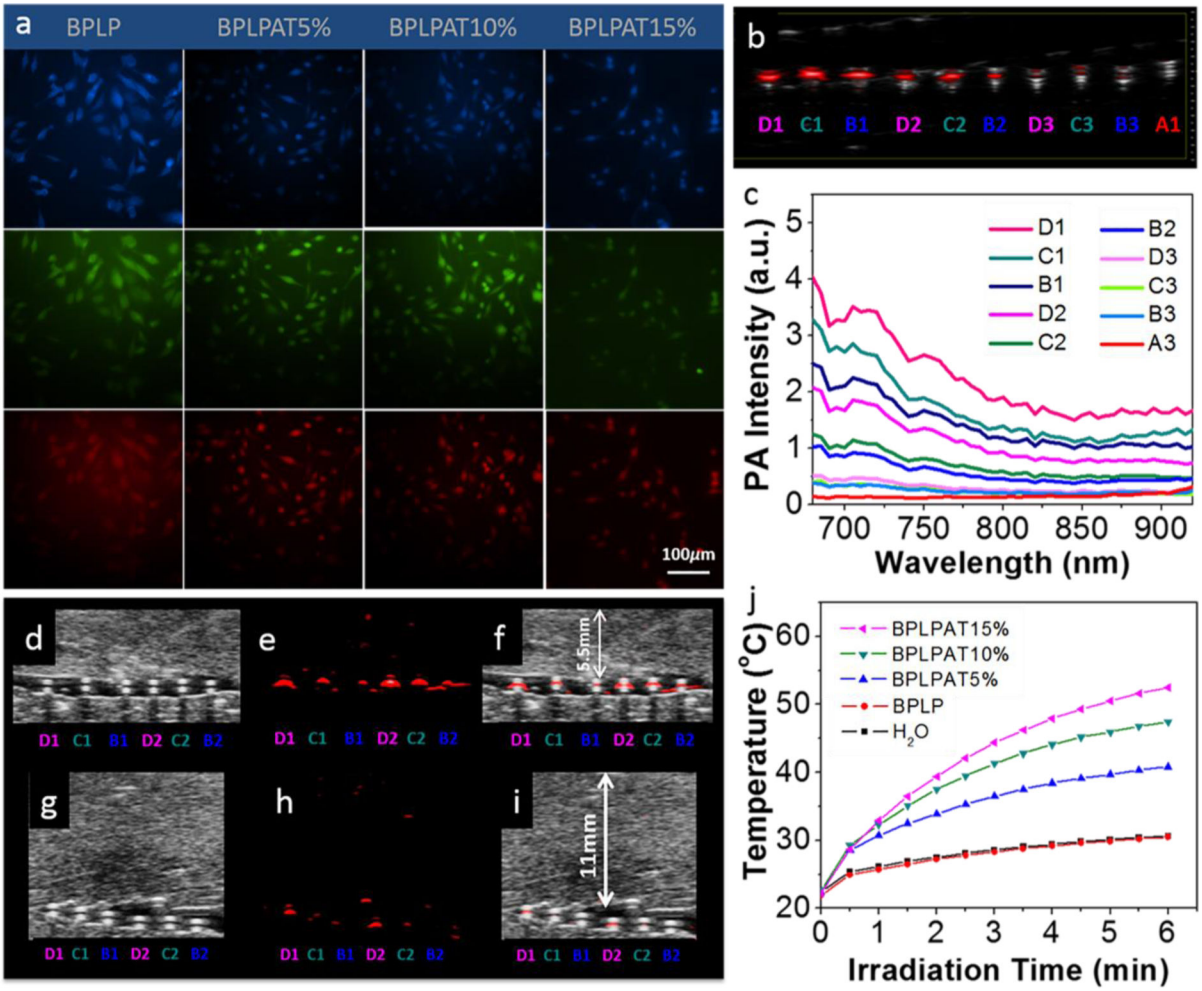

Figure 5.

Fluorescence imaging, PA imaging, and photothermal capabilities of BPLPAT nanoparticles. (a) Fluorescent images of PC12 cells uptaken with BPLP and BPLPAT nanoparticles with blue, green, and red fluorescence. (b) Superimposed ultrasound and PA images of BPLP and BPLPAT nanoparticle solutions in plastic tubes in water medium at various concentrations. (c) PA intensity of BPLP and BPLPAT nanoparticle solutions at various concentrations. (d) Ultrasound images, (e) PA images, and (f) superimposed ultrasound and PA images of BPLP and BPLPAT nanoparticles under a 5.5 mm thick layer of chicken breast tissue. (g) Ultrasound images, (h) PA images, and (i) superimposed ultrasound and PA images of BPLP and BPLPAT nanoparticles covered under a 11 mm thick layer of chicken breast tissue. (j) Temperature rise traces of the BPLP and BPLPAT nanoparticles at a concentration of 0.5 mg/mL under NIR illumination, DI water works as the control. (BPLPAT15% 2mg/mL(D1), BPLPAT10% 2mg/mL(C1), BPLPAT5% 2mg/mL(B1), BPLPAT15% 1mg/mL(D2), BPLPAT10% 1mg/mL(C2), BPLPAT5% 1mg/mL(B2), BPLPAT15% 0.5mg/mL(D3), BPLPAT10% 0.5mg/mL(C3), BPLPAT5% 0.5mg/mL(B3), BPLP 2mg/mL(A1).

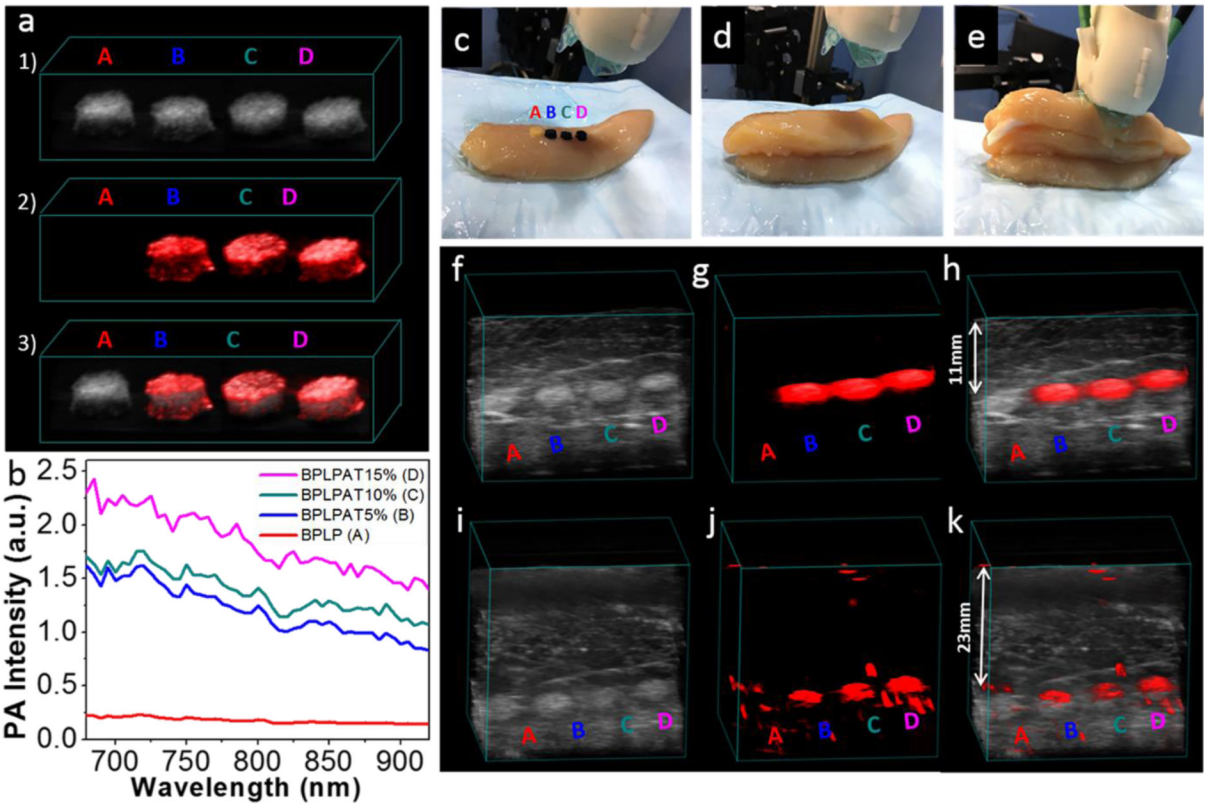

Figure 6.

PA imaging of BPLP and BPLPAT scaffolds. (a) (1) Ultrasound images, (2) PA images, and (3) superimposed ultrasound and PA images of BPLP and BPLPAT scaffolds embedded inside agar gel. (b) PA intensity of BPLP and BPLPAT scaffolds. (c), (d), and (e) Experiment setup for deep tissue PA imaging of BPLP and BPLPAT scaffolds. (f) Ultrasound images, (g) PA images, and (h) superimposed ultrasound and PA images of BPLP and BPLPAT scaffolds covered under a ~11 mm thick layer of chicken breast tissue. (i) Ultrasound images, (j) PA images, and (k) superimposed ultrasound and PA images of BPLP and BPLPAT scaffolds covered under two layers thick (total ~23 mm thick) of chicken breast tissue.

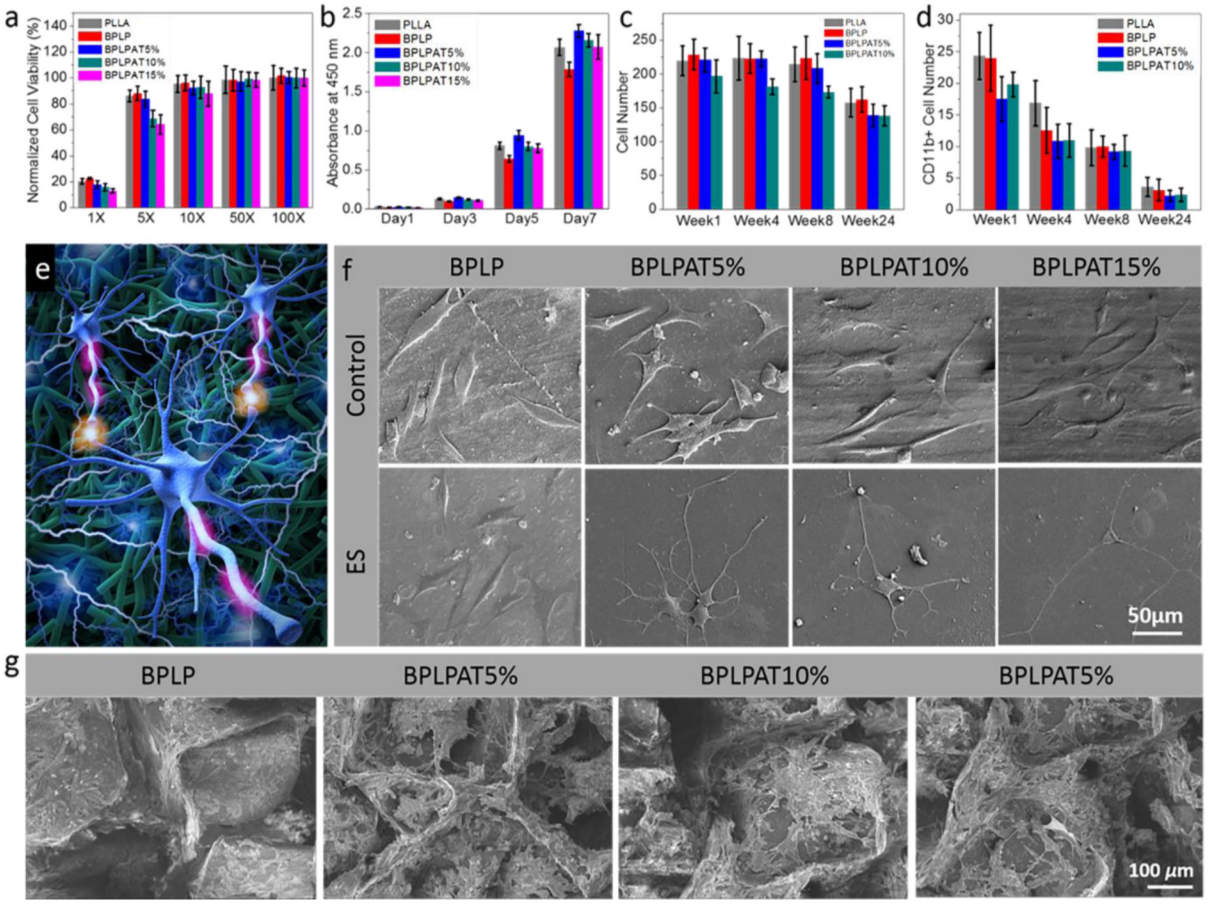

Figure 7.

In vitro cell culturing and *in vivo* foreign body response studies on BPLPAT materials. (a) Cytotoxicity of degradation products of BPLP and BPLPATs, PLLA film as a control. (b) PC12 cell proliferation studies on BPLP and BPLPAT films for 7 days, PLLA film as a control. (c) Averaged total and (d) CD11b positive cell numbers in a 200 × 200 μm^2 square region near the implant films. (e) Schematic of electrical stimulation of PC-12 cells on crosslinked BPLPAT materials. (f) SEM images of PC-12 cells on BPLP and BPLPAT films without electrical stimulation (control) and with electrical stimulation (ES). (g) SEM images of PC-12 cells on BPLP and BPLPAT scaffolds with electrical stimulation.

Table 1.

Conductivity of BPLP and BPLPAT films

Samples	Conductivity (S/cm)
BPLP	N/A
BPLPAT5%	1.06×10^{-7}
BPLPAT10%	4.32×10^{-7}
BPLPAT15%	2.94×10^{-6}

Table 2.

Size and Zeta potential of BPLP and BPLPAT nanoparticles.

Nanoparticles	BPLP	BPLPAT5%	BPLPAT10%	BPLPAT15%
Size (nm)	164.3 ± 6.9	178.2 ± 4.3	182.6 ± 2.0	181.9± 5.7
Zeta potential (mV)	−55.5 ± 2.0	−60.2 ± 0.6	−59.3 ± 2.8	−49.1± 0.7